Automation in Construction 141 (2022) 104446

Contents lists available at ScienceDirect

Automation in Construction

journal homepage: www.elsevier.com/locate/autcon

Road marking degradation analysis using 3D point cloud data acquired with a low-cost Mobile Mapping System

Mario Soilán [a,*], Diego González-Aguilera [a], Ana del-Campo-Sánchez [a], David Hernández-López [b], Susana Del Pozo [a]

[a] Department of Cartographic and Land Engineering, Higher Polytechnic School of Ávila, Universidad de Salamanca, Hornos Caleros 50, 05003 Ávila, Spain
[b] Institute of Regional Development, University of Castilla-La Mancha, 02071, Albacete, Spain

ARTICLE INFO

Keywords:
Mobile LiDAR system
3D point cloud
Road markings
Road maintenance
Retroreflectivity degradation

ABSTRACT

Road maintenance is an important task that ensures the availability and correct function of the road infrastructure. This work presents a methodology that, first, offers an empirical radiometric analysis of the Velodyne VLP-32C laser scanner. Second, it defines a road marking degradation model that estimates the coefficient of retroreflected luminance (night visibility, R_L) using the intensity attribute of 3D point clouds acquired with this low-cost system. This model is validated and applied to a case study road section of about 6 km in length, where a continuous degradation map is defined together with data to assist decision-making for preventive and corrective maintenance. This validation shows that the proposed method is capable of offering good qualitative visualizations of the degradation status of the road markings, as well as detecting those areas with high degradation (R_L< 100 mcd/m^2/lx) that require corrective maintenance.

1. Introduction

Transport infrastructure is a key asset in our society, and a crucial sector of the economy. According to data from the European Commission [1], the transport and storage services sector accounts for about 5% of total gross value added (GVA) in the EU-27 in 2019, employing around 10.5 million persons, a 5.4% of the total workforce. In Spain, according to the Ministry of Transportation, Mobility, and Urban Agenda, the road network has 165,445 km, of which 17,377 km are high-capacity roads. Proper maintenance of such a large infrastructure is becoming a great challenge, since investment and maintenance budgets are typically subjected to the economic climate and political decisions. In Spain, the maintenance budget reached a minimum in 2018 (786 million €) under a context of an infrastructure conservation deficit. This negative trend is being slowly corrected, and the budget in 2022 has been increased to 1.371 million €, which sets a historical maximum for road maintenance. The development and integration in the market of remote sensing surveying technologies and equipment are slowly shifting the concept of infrastructure maintenance.

A well-established remote sensing technology that can be used to improve road maintenance activities is laser scanning. This technology can be employed to scan the environment from a static position (Terrestrial laser scanner – TLS -) or in an airborne setting, embedded in a drone or aircraft (aerial laser scanner – ALS -), but the proper setting for road inspection and maintenance comes from the integration of this technology in terrestrial vehicles. When it is part of a system that integrates positioning sensors (Global Navigational Satellite System – GNSS and Inertial Measurement Unit – IMU) and, optionally, other sensors (photographic or even thermographic cameras), it is usually called Mobile Mapping System (MMS) or Mobile LiDAR System (MLS). There are several reviews partially or totally dedicated to methods and applications of MMS/MLS data for road infrastructure [2–6] that illustrate the versatility and the capabilities of this technology. In essence, a MMS/MLS can acquire precise, three-dimensional (3D) representations of the surveyed infrastructure in the form of metric point clouds. Although initially unstructured and with no topological relation among its points, the large amount of geometric and radiometric data that can be collected in a 3D point cloud (up to millions of points per second), enables the development of a wide range of infrastructure inspection, inventory, and maintenance applications. Some relevant and recent examples in the literature show the capabilities of this technology for detecting the road platform and its layout [7–9], pole-like objects [10],

* Corresponding author.
E-mail addresses: msoilan@usal.es (M. Soilán), daguilera@usal.es (D. González-Aguilera), ana.delcampo@usal.es (A. del-Campo-Sánchez), David.hernandez@uclm.es (D. Hernández-López), s.p.aguilera@usal.es (S. Del Pozo).

https://doi.org/10.1016/j.autcon.2022.104446
Received 16 February 2022; Received in revised form 16 June 2022; Accepted 17 June 2022
Available online 24 June 2022

guardrails [11] or power lines [12], among others.

Given the objectives of this work, applications related with road markings are of special relevance. Detecting and classifying road markings using 3D point clouds is a problem that has been addressed in the literature. The most common approaches rely on the intensity attribute of the point cloud, which is analysed in order to find the position of the road markings on the ground [13,14], and it has been proven that approaches based on Deep Learning obtain the best results, such as those presented in the work of Wen et al. [15], where road markings are not only detected and classified but also completed, finding occlusions and misdetections with a conditional generative adversarial network (cGAN). Another example is the work of Ma et al. [16], which uses a capsule-based Deep Learning framework for road marking extraction and classification from MMS point clouds.

While the objective of these works is the detection of road markings, they do not study their conservation status, that is, they offer the position or the semantics of the road markings, but they do not offer relevant maintenance information related with the degradation of the markings. Here, the intensity attribute of the point cloud is also a key property. In [17], this attribute is defined as the amplitude of the return signal of the LiDAR, which can be the analogue electrical signal output from the photodetector or the digitized waveform. However, they state that this definition may be inconsistent with strict radiometric usage. In a 3D point cloud encoded in a .las file, the intensity is typically discretized to an 8-, 12- or 16-bit dynamic range, and it is a relevant parameter to extract information about the surfaces. The factors that influence the measurement of intensity values have been studied in the remote sensing literature and can be summarized as (1) reflectance [18], (2) surface roughness [19], and acquisition geometry (range and angle of incidence) [20,21]. To correct the intensity measurements considering these parameters, there are different methods in the literature. Typically, theoretical models define corrected intensity measurements as a function of range and angle of incidence [22,23], which leads to values proportional to the surface reflectance.

Since the quality of road markings is given by their reflective properties, this sets a path for using 3D point cloud data acquired by MMS/MLS to assist in the maintenance and inspection of road markings. Burghardt et al. [24] tested different road marking materials and glass beads under different laboratory conditions using LiDAR and cameras, and measured the correlation between the luminance coefficient under diffuse illumination (Q_d), the coefficient of retroreflective luminance (R_L) and LiDAR intensity. While they found a correlation with R_L, the correlation with Q_d was weak. This is consistent with the definition of the intensity attribute on a LiDAR point cloud, as Q_d is related with the visibility of the road marking during daytime and R_L with the retroreflection, and therefore has an impact on the amplitude of the return signal of the LiDAR.

In practice, R_L measurements are obtained using retroreflectometers. While some companies still perform static measurements, there are dynamic retroreflectometers that can be installed in a vehicle that drives at conventional speeds. Studies show that both static and dynamic analyses yield comparable results, although different interpretations of them may be obtained, depending on differences in the test procedures [25]. Although the existence of methods for dynamic retroreflectivity testing may question the relevance of using a MMS, two clear advantages justify this research: (1) Dynamic retroreflectometers are dedicated equipment that can be used only for road marking maintenance. However, data collected by a MMS can assess multiple inventory and maintenance issues, as has been introduced in this section. Thus, with the same equipment, not only road markings can be assessed, but also traffic signs, bridge/tunnels clearances, and structural health or pavement roughness among others. (2) Dynamic test methods are characterized by higher initial costs and measurement costs [25], which causes some companies to still perform static measurements. In this context, it is also worth mentioning the research by Olsen et al. [26] who present a complete report where they use a Leica Pegasus MMS, develop algorithms for extracting road markings from the 3D point cloud, and then calibrate the system for quantifying the retroreflectivity degradation of the markings. They state that using mobile LiDAR point clouds can be a safe, cost-effective, and reliable solution to provide accurate estimates of retroreflectivity for pavement markings.

While the scope of this work cannot be as wide as that report, the objective is similar: To perform an empirical radiometric analysis on a low-cost MLS and to develop degradation models to estimate the retroreflectivity of road markings from the intensity measurements on the 3D point cloud. Furthermore, these results can be applied to generate degradation maps of the road, assisting the decision-making processes of end-users (road maintenance and conservation companies) by exporting qualitative and quantitative degradation-related data.

In line with these objectives, the contributions presented in this paper can be summarized as:

1. A radiometric analysis of a low-cost MLS equipped with a Velodyne VLP-32C laser scanner, and the development of a model to estimate the degradation of the road markings.
2. A workflow that takes the first contribution into practice and generates cartographic degradation maps that can be easily visualized on Geographical Information System (GIS) software. Furthermore, data to assist decision-making processes according to the requisites of the end-users of this work are part of the output of this workflow.

2. Case study data

The 3D point cloud data employed in this work has been acquired with a customized assembly of the Phoenix Scout Ultra 32 Mobile LiDAR System (Fig. 1a). It is a lightweight, low-cost system equipped with a Velodyne VLP-32C laser scanner, that has 32 laser beams, with a horizontal and vertical field of view of 360° and 40°, respectively. The scanner operates at a wavelength of 903 nm, and it is able to get dense point clouds with a scan rate of 600,000 measurements per second. The complete specifications of the scanner can be found in the reference [27]. This system was mounted in a van with an inclination of approximately 45°, and the global positioning was done with a single-antenna, dual-frequency RTK-GNNS receiver, whose position with respect to the laser and IMU is known and calibrated. A GNSS Topcon HiPer V, placed at <15 km from the trajectory, was used as a base for trajectory post-processing with Inertial Explorer. Data acquisition took place in three different roads in Spain, near the cities of Albacete, Valladolid, and Ávila (Fig. 1c-e). Field work related with datasets 1 (Albacete) and 2 (Valladolid) consisted of data acquisition for the definition of the degradation model defined in Section 4.2. Roads from these survey locations have sections with one or two lines for each direction and showed different levels of degradation along the surveyed length. The field work related to dataset 3 (Ávila) was carried out on a conventional road, and the data was used for the validation of the model. Information from those surveys is summarized in Table 1.

In parallel to the mobile LiDAR survey, a retroreflectometer was employed to measure the coefficient of retroreflected luminance (night visibility, R_L, measured in mcd/m^2/lx) of road markings (Fig. 1b), with a resolution of 1 mcd/m^2/lx, a measuring area of 50x100mm, an observation angle of 2.29° and an illumination angle of 1.24°. It can be used regardless of light conditions, and it is able to measure the visibility of both dry and wet road markings. In this work, a set of measures were manually recorded in different road marking surfaces along the case study area, annotating the R_L values displayed by the retroreflectometer as well as an accurate GNSS position of the measured areas, so these measures could be georeferenced with respect to the 3D point cloud data. Note that the coefficient under diffuse illumination (Q_d) is not utilized in this work as it does not correlate with the intensity measurement from the LiDAR system, as reported in the literature [24]. Furthermore, only white markings were considered in this study, and the field work was done under clear meteorological conditions, as

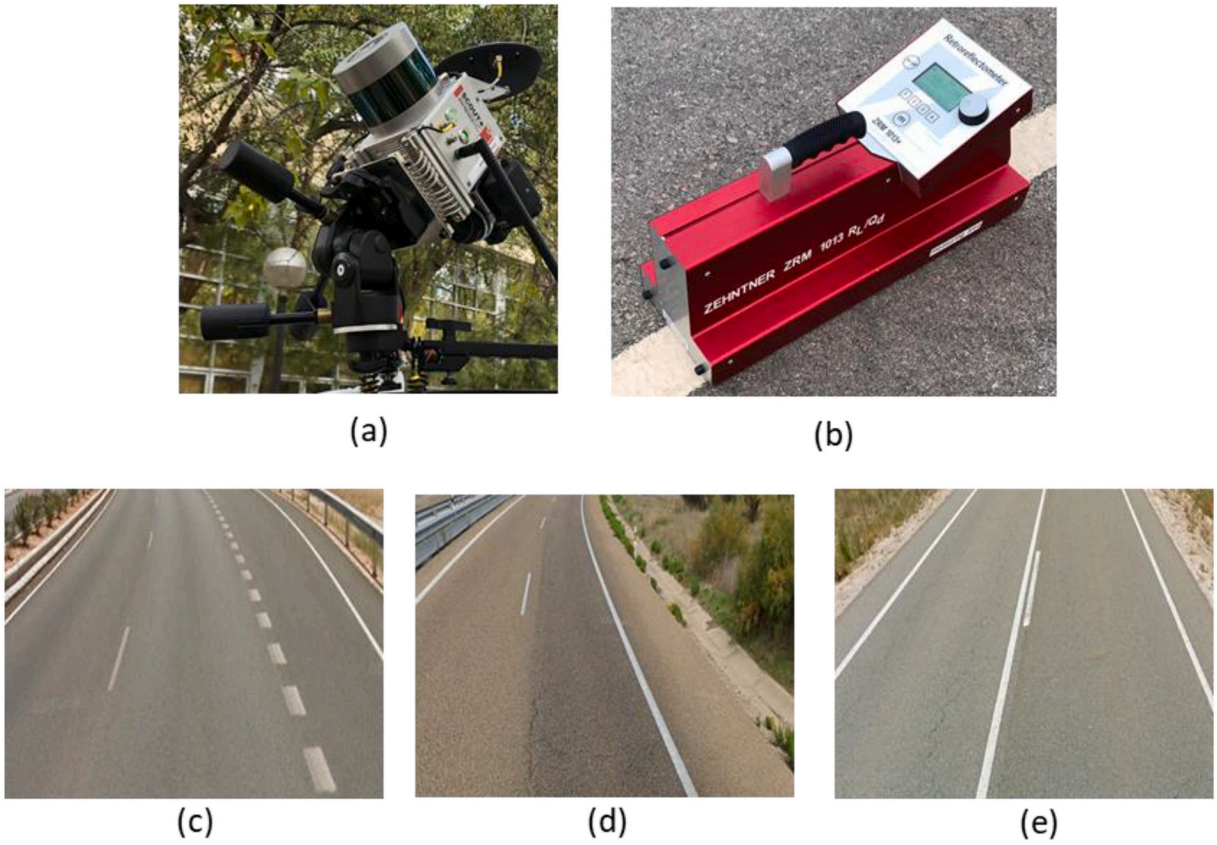

Fig. 1. Case study data. (a) MMS equipped with GNSS-INS and a Velodyne VLP-32C laser scanner, used for the presented surveys. (b) Retroreflectometer used to collect R_L ground truth data (c-e) Survey locations: Albacete (CM-3203), Valladolid (N-601), Ávila (AV-110).

Table 1
Case study data from three different locations in Spain.

Survey Location	Survey Length	Usage
1 – Albacete (CM-3203)	10 km	Model fit
2 – Valladolid (N-601)	10 km	Model fit
3 – Ávila (AV-110)	6 km	Model validation

conditions such as fog significantly affect LiDAR performance [28].

3. Methods

This section presents the methodological approach of this work. First, the 3D point cloud data from the case study is processed in order to extract intensity-related information. A hypothesis for an intensity correction algorithm is set and validated, and a degradation model is defined. Finally, that model is employed to define a degradation map which served as validation of the case study.

3.1. Data preparation

Let $\mathcal{P} = (x, y, z, I, t_s)$ be the 3D point cloud acquired by the MLS presented in Section 2, where the coordinates of each point (x, y, z) have attributes such as intensity (I) and time stamp (t_s). Furthermore, let $\boldsymbol{P_m}$ be a list of 3D coordinates that represent the points where R_L measurements of road markings were carried out.

To prepare the data for further processing, it is important to note that most of the information from the 3D point cloud is not needed in a first step as the objective is to analyse the intensity values of the point cloud in the areas measured in the field. Therefore, a process that selects and isolates the local surroundings of each measured area is needed. For large point clouds, neighbourhood search may be computationally intensive, as point distances need to be computed for every point in the cloud in order to obtain the neighbourhood of a single points. Thus, a faster and less demanding process based on rasterization is proposed.

First, the 3D point cloud $\mathcal{P}$ is rasterized by projecting its 3D coordinates into the XY plane, where a uniform grid is defined. Each point will be located within a cell of the grid, and each cell will have an index, such that the set of points within any raster cell are unambiguously identified with the correspondent cell index. Then, if the points in $\boldsymbol{P_m}$ are also projected on the same grid, the cells that contain any point from $\boldsymbol{P_m}$ can be selected to extract points from $\mathcal{P}$ on those cells. To avoid cases where local information is lost due to $\boldsymbol{P_m}$ lying close to the border of the raster cell, the neighbouring cells are also selected. That is, for each R_L measure, whose position is recorded in $\boldsymbol{P_m}$ (Fig. 2a), a 3D point cloud is extracted from $\mathcal{P}$, containing the local neighbourhood of the measured area. For this work, the grid cell for the rasterization process has been defined as $g_r = 2$ m. Therefore, this process outputs a set of 3D point clouds $\boldsymbol{P}_{marking} = (\boldsymbol{P}_1 \ldots \boldsymbol{P}_i \ldots \boldsymbol{P}_N) | \, \boldsymbol{P}_i \in \mathcal{P}$, such that each of them cover a 6 $\times$ 6 m area on the plane, with the point where the retroreflectivity was measured approximately lying in the centre of the cloud (Fig. 2b).

3.2. Radiometric analysis of the VLP-32C scanner

The first step of the methodology is to perform an analysis of the radiometric behaviour of the VLP-32C laser scanner. The initial hypothesis is supported in reference [17], where a theoretical correction is presented as a common method to compensate for variation in intensity data caused by range (distance between sensor and target, R) and angle of incidence (angle between the beam and the target, α) following Eq. 1:

$$I_c = I \cdot \frac{R^2}{R_{ref}^2} \cdot \frac{1}{cos\alpha} \tag{1}$$

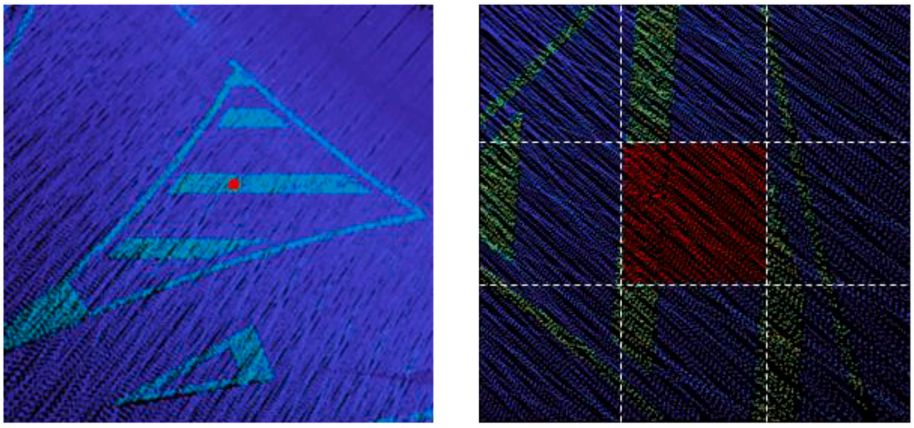

Fig. 2. Data preparation. **(a)** Section of the 3D point cloud $\mathcal{P}$, where the GNSS coordinates of one of the R_L measurements from $\boldsymbol{P_m}$ is visualized in red over the road marking. **(b)** After a rasterization process, the raster cell that contains the GNSS coordinates of the measurement (coloured in red) as well as its neighbouring cells, are extracted. (For interpretation of the references to colour in this figure legend, the reader is referred to the web version of this article.)

where I and I_c are the raw and corrected intensities, respectively, and R_{ref} is a user-defined reference range, such that the corrected values are equivalent to those intensities measured from that reference range.

However, the suitability of this equation should be verified, as currently there is no standard approach for intensity correction across manufacturers. For instance, some scanners have brightness reducers for near distances [17] that invalidate the intensity correction shown in Eq. 1. Furthermore, there is not a clear insight on the radiometric behaviour of the scanners [20]. The VLP-32C codifies the intensity on 8 bits, thus it is stored in a variable with 256 possible values. Furthermore, according to the manufacturer, the reflectivity measurements should be independent of laser power and distances involved. The hypothesis set in this section will empirically test that behaviour.

3.2.1. Laser positioning

It is important to note that the parameters (R, α), required for intensity correction, cannot be computed in a straightforward manner, as the position of the laser is initially unknown. However, it is possible to estimate this position given:

- The trajectory of the vehicle, as recorded by the navigation system, $\mathcal{T} = (x, y, z, t_s)$, including cartographic Universal Transverse Mercator (UTM) 3D coordinates (x, y, z) and a time stamp, t_s, for each 3D point. Note that the trajectory is recorded with a frequency of 1 Hz, therefore there is a single point registered per second.
- The orientation of the laser based on the IMU, as roll, pitch and yaw angles (ϕ, θ, ψ) for each point of the trajectory.
- The distance between the GNSS antenna and the IMU, measured in the coordinate system of the latter. Let it be defined in meters as $d_{gi} = (0.019301, 0.2405, -0.03943)$.
- The distance between the IMU and the laser, as specified by the specification sheet of the manufacturer, measured in the same coordinate system as d_{gi}. Let it be defined in meters as $d_{il} = (0, -0.04655, -0.04593)$. Thus, the distance between the laser and the GNSS antenna can be defined as $d_{gl} = d_{gi} + d_{il}$.
- The rotation matrix between the reference system of the GNSS and the IMU, R_{gi}.

To estimate the position of the laser, let $p_i = (x_i, y_i, z_i, t_{si})$ be any point within the 3D point cloud data acquired for this study. As mentioned, the trajectory is recorded with a frequency of 1 Hz, but the point cloud data has a greater acquisition rate. For that reason, it is necessary to interpolate the coordinates of the trajectory for each point. First, the two closest time stamps to t_{si} (before and after the acquisition of the point) are selected, defining two trajectory positions $t_1 = (x_1, y_1, z_1, t_{s1})$ and $t_2 = (x_2, y_2, z_2, t_{s2})$. Then, the interpolated trajectory position for p_i is obtained following Eq. 2, where the interpolation distance d_{interp} is computed following Eq. 3. Note that the lineal interpolation assumes a constant speed of the vehicle in the time interval $[t_{s1}, t_{s2}]$.

$$t_i = t_1 + d_{interp}(t_2 - t_1) \tag{2}$$

$$d_{interp} = \frac{t_{si} - t_{s1}}{t_{s2} - t_{s1}} \tag{3}$$

This interpolation process is also applied to the orientations recorded on the trajectory positions t_1 and t_2. Thus, for an interpolated trajectory position t_i, orientations $(\phi_i, \theta_i, \psi_i)$ are computed.

Then, the transformation matrix, T, required to estimate the coordinates of the laser given a trajectory position t_i, is defined as shown in Eqs. 4–5. It performs a rotation according to the matrix R_{gi} and orientations given by the IMU (R_i), and a translation that positions the origin of the transformed reference system in t_i.

$$T = \begin{pmatrix} R_{gi} \cdot R_i & t_i \\ 0_{1x3} & 1 \end{pmatrix} \tag{4}$$

$$R_i = \begin{pmatrix} cos\phi_i & -sin\phi_i & 0 \\ sin\phi_i & cos\phi_i & 0 \\ 0 & 0 & 1 \end{pmatrix} \begin{pmatrix} 1 & 0 & 0 \\ 0 & cos\theta_i & -sin\theta_i \\ 0 & sin\theta_i & cos\theta_i \end{pmatrix} \begin{pmatrix} cos\psi_i & 0 & -sin\psi_i \\ 0 & 1 & 0 \\ sin\psi_i & 0 & cos\psi_i \end{pmatrix} \tag{5}$$

This way, the positioning of the laser p_l can be expressed in the same system of reference as any point of the 3D point cloud p_i, given the vector d_{gl} that measures the offset between t_i and p_l in the IMU system of reference (Eq. 6).

$$p_l = T \cdot d_{gl} \tag{6}$$

3.2.2. Intensity correction

Once the position of the laser can be estimated for all the points in the 3D point cloud, the theoretical intensity correction model presented in Eq. 1 can be implemented for each single point. It requires the calculation of two parameters: The distance between the laser and the target (R) and the angle of incidence between the beam and the target (α) (Fig. 3a). Given any point p_i from the 3D point cloud, and the estimated position of the laser when that point was acquired, p_l, the distance R is straightforwardly computed as the Euclidean distance between both 3D coordinates (Eq. 7). The angle of incidence α is computed as the angle

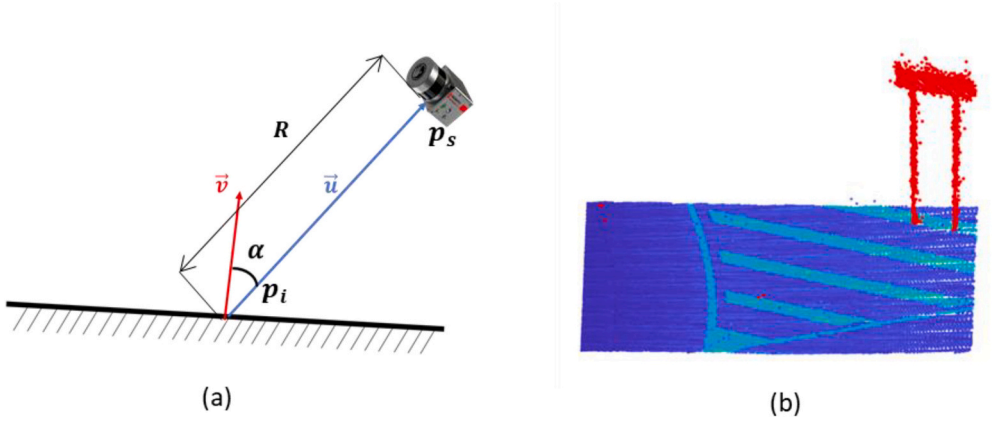

Fig. 3. **(a)** The distance R and the angle of incidence α are computed for each point p_i and its correspondent laser position p_l. **(b)** The normal vector $\vec{v}$ is computed applying PCA to the road surface points, after filtering out off-ground points (coloured in red). (For interpretation of the references to colour in this figure legend, the reader is referred to the web version of this article.)

between a vector that represents the beam ($\vec{u}$) and the normal vector of the surface where target point p_i is located ($\vec{v}$) (Eq. 8).

$$R = ||p_i - p_s|| \tag{7}$$

$$\alpha = \text{acos}\ \frac{\vec{u}\cdot\vec{v}}{|\vec{u}\cdot\vec{v}|} \tag{8}$$

Note that the definition of the normal vector $\vec{v}$ is not straightforward. As detailed in Section 3.1, each point cloud from $\boldsymbol{P}_{marking}$ covers a 6 × 6 m area on the plane. Thus, the surface plane can be defined by applying Principal Component Analysis (PCA) to those points in $\boldsymbol{P}_i$ that belong to the road surface. This requires an additional processing step: The point cloud $\boldsymbol{P}_i$ may contain off-ground points such as traffic signs or other objects (Fig. 3b) that must be filtered out before defining the road surface. For that reason, a local normal vector is estimated for each point $p_i \in \boldsymbol{P}_i$, fitting a plane for a neighbourhood composed of the 50 closest points to p_i. While these normal vectors are noisy (which is a strong reason to justify using a single normal vector for each $\boldsymbol{P}_i$), the value of their vertical components can be used to filter out points that do not belong to the road surface. Here, a threshold value of 0.9 is stablished, so normal vectors with lower vertical component are discarded (Fig. 3b). Note that this simple approach is valid as point clouds $\boldsymbol{P}_i$ cover a small surface whose slope can be considered constant, but it will likely fail for larger point clouds.

Once the road surface is segmented, the third eigenvector obtained with PCA will be considered as the surface normal, thus it will be vector $\vec{v}$ for the calculation of the angle of incidence α for all points in $\boldsymbol{P}_i$.

Finally, the theoretical intensity correction from Eq. 1 can be applied point by point to each point cloud in $\boldsymbol{P}_{marking}$. Measuring the range values of the complete dataset, it can be seen that the majority of the points have values between 5 and 10 m. Therefore, the reference range R_{ref} in Eq. 1 is set as 6 m. The raw intensity values are normalized in the range [0,1]. Fig. 4 shows the same point cloud with raw and corrected intensity values.

The colour map in Fig. 4 gives a visual representation of the theoretical intensity correction effect. As it can be seen, the initial hypothesis set in Section 3.2 may not be correct, as the expected uniformity on the corrected intensity values for a local area of a road marking does not exist, hence this theoretical correction may not be suitable for the laser employed. In order to validate this statement, the following analysis is carried out: First, a subset of $\boldsymbol{P}_{marking}$ is defined by randomly selecting a number of individual point clouds $\boldsymbol{P}_i$. Then, road markings on each point cloud are segmented, setting a single threshold for the raw intensity values, and checking the results manually, slightly adjusting the threshold value if necessary. Finally, the relation between the raw and corrected intensities with the range and angle of incidence parameters is studied for all the road markings points in the data subset. The outcomes of this analysis are shown in Section 4.1 from the results.

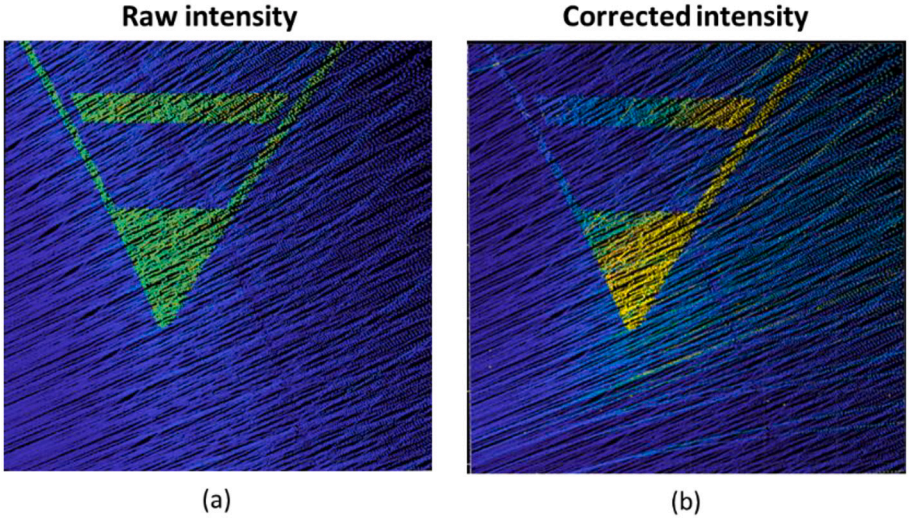

Fig. 4. Intensity correction. **(a)** Point cloud $\boldsymbol{P}_i$ coloured by its raw intensity values. **(b)** Point cloud $\boldsymbol{P}_i$ coloured by its corrected intensity values.

The new hypothesis that is set at this point is that, given the radiometric behaviour of the LiDAR system on the studied areas, it may be possible to stablish a correlation between the raw intensity values and the coefficient of retroreflected luminance as measured on field.

3.3. Modelling intensity values

Once the radiometric behaviour of the LiDAR system has been analysed, the next step, given the results obtained in Section 4.1, is to find a model that fits the raw intensities as acquired by the LiDAR system, and the coefficient of retroreflected luminance (R_L) as measured in the field by a retroreflectometer as described in Section 2. For that purpose, each point cloud $\boldsymbol{P}_i$ from the set $\boldsymbol{P}_{marking}$ is processed as follows: First, the GNSS positions from $\boldsymbol{P}_m$ that were used to generate $\boldsymbol{P}_i$ are retrieved, and then, points in $\boldsymbol{P}_i$ whose distance with that coordinates is <10 cm are selected, and the average raw intensity of those points is computed. This is done for two reasons: (1) reducing the noise of a single measure by averaging neighbouring points, and (2) accounting for the positioning accuracy of the GNSS device that recorded coordinates $\boldsymbol{P}_m$ as well as for the measurement area of the retroreflectometer. In order to avoid outliers where the selected points do not completely belong to a road marking area, this process is manually supervised.

Then, a set of pairs (I_{raw}, R_L) is obtained. In Section 4.2, it can be seen that, qualitatively, there is a positive, non-linear correlation between both values. After an empirical analysis, it was found that a single-term power model (Eq. 9) could be used to fit the data (Section 4.2).

$$R_L = a \cdot I_{raw}^{b} \tag{9}$$

3.4. Data representation for preventive and corrective maintenance

Once the intensity of a 3D point cloud is expressed in terms of night visibility (R_L), it can be employed for preventive maintenance of the road markings. According to the Spanish guide for project and execution of road marking works [29], which is supported by the norm UNE-EN 1436, there are different levels of service for road markings, that are summarized in Table 2. It establishes different retroreflectivity classes that should meet the temporal specifications on the normative. Furthermore, this guide stablishes, as a preventive maintenance criterion, a R_L value of 150 mcd/m^2/lx. In practice, road marking repainting is carried out when the R_L value of any marking of a road section (which may vary in length) has a value $\leq$ 100 mcd/m^2/lx.

Given these data, the 3D point cloud can be used to support corrective and preventive maintenance tasks. However, it is important to note that, even if the intensity values of a point cloud can be translated to retroreflectivity values, road markings must be located in the point cloud in order to analyse them, which is a non-trivial step given the unstructured nature of 3D point cloud data.

Fig. 5 shows a workflow that summarizes the process to export meaningful information for road marking maintenance from an input 3D point cloud. First, a road marking segmentation process is applied to filter out points that do not belong to road markings. This process, which is out of the scope of this work, can be manual, based on heuristics or on Machine Learning algorithms. Then, the R_L values of each point can be retrieved from the model defined in Section 4.2.

Subsequently, it is necessary to subsample the resulting point cloud, as the point density is too high to offer an efficient visualization of the data. For that reason, the point cloud that contains the road markings is rasterized (projecting the point cloud on the XY plane) with a grid size of $1m^2$, and a single point is chosen for each raster cell as the closest point to the cell centroid. Then, the R_L value of that point will be computed as the average R_L value of the road marking points on a neighbourhood of 1 m of radius. This process intends to reduce the noise of individual measures and to improve the qualitative results of the visualization, as it is shown in Section 4.3. Finally, a degradation index is assigned to each point according to the R_L value, and the percentage of points with $R_L \leq$ 100 mcd/m^2/lx is computed for each 100 m of road. Note that this process is completely automatic, with no manual intervention. If a set of relevant coordinates for the maintenance of road markings were known beforehand, the process could be simplified, but a local road marking segmentation would still be needed to get a proper R_L estimation.

Table 2
Levels of service for road markings, for the parameter R_L according to national guidelines.

	Night visibility		
	30 days	180 days	730 days
R_L mcd/m^2/lx	≥300 (*R*5)	≥200 (*R*4)	≥100 (*R*2)

4. Results

4.1. Radiometric analysis

In Section 3.2, the radiometric analysis of the VLP-32C laser scanner is carried out under an initial hypothesis from Eq. 1. As stated in the literature, theoretical corrections of the intensity values within a 3D point cloud show a relation between the raw intensity value and the range and angle of acquisition for each point. Nonetheless, the process in Section 0 showed that this initial hypothesis may not be correct for the laser employed, as the corrected intensity was qualitatively inaccurate over the studied areas. To quantify this and to obtain empirical conclusions, road markings are segmented from a subset of $N = 7$ 3D point clouds from $\boldsymbol{P}_{marking}$ (Fig. 6a). This subset contains 49,584 points and covers a complete interval of the parameters (R, α): Here, these intervals are $R \in [2.3\text{ m}, 16.1\text{ m}]$ and $\alpha \in [30.5^{\circ}, 82.7^{\circ}]$. In Fig. 6b, different visualizations of the data are shown using the N point clouds of the data subset. There, it can be seen that there is not a correlation between raw intensity values and (R, α) parameters. In fact, the raw intensity is relatively stable across the dataset. Consequently, the application of the theoretical intensity correction equation outputs an intensity distribution that is clearly correlated with (R, α) parameters, given the intensity correction from Eq. 1.

To quantify this, Pearson's linear correlation coefficient is computed for (R, α) parameters with respect to the raw and corrected intensity, for all observations in the data subset. Table 3 shows the results, that corroborate the qualitative conclusions extracted from the data in Fig. 6b. It is clear that the raw intensity values are not correlated with the parameters from the theoretical correction, therefore the initial hypothesis set in Section 3.1 has to be discarded.

4.2. Degradation model

As stated in Section 3.3, a single-term exponential model was found the best option to fit the (I_{raw}, R_L) data (Eq. 9). As introduced in Section 2, the case study consists of three surveys in different locations and seasons of the year. The road was dry during all the surveys, except for one where it rained the night before the data acquisition. However, this fact had no impact on the data collected from the field work.

Following the process outlined in Section 3.3, a set of pairs (I_{raw}, R_L) is obtained using data from dataset 1 (Albacete) and dataset 2 (Valladolid). During the process, some of the retroreflectometer measurements were discarded due to lack of information in the point cloud (occlusions or lack of point cloud data on the measured zone). A total number of 63 data pairs (I_{raw}, R_L) are considered to fit the model. Using the curve fitting app from MATLAB®, a robust non-linear least squares fitting is applied to the data. Different configurations are tested to find the best model. Since least squares is sensible to outliers, and the set of (I_{raw}, R_L) points is considerably noisy, two robust methods are tested: (1) Least Absolute Residuals (LAR), which minimizes the absolute difference of the residuals rather than the squared differences, and (2) Bisquare weights, that minimized a weighted sum of squares. Two fitting

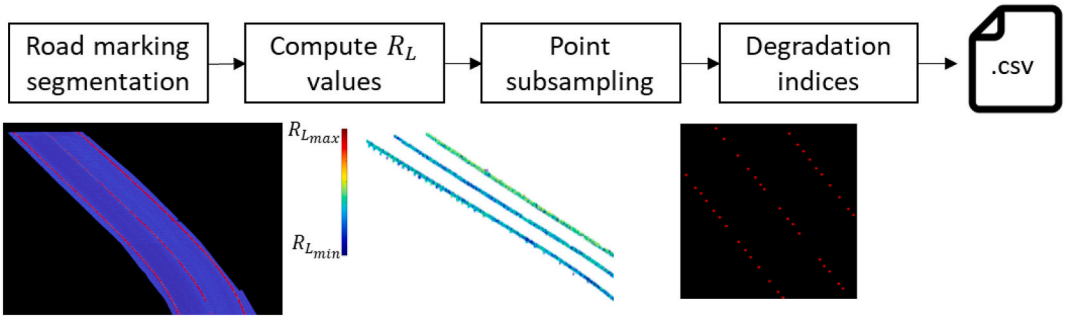

Fig. 5. Point cloud processing workflow. It takes a 3D point cloud and the degradation model as input and exports a degradation map of the road markings.

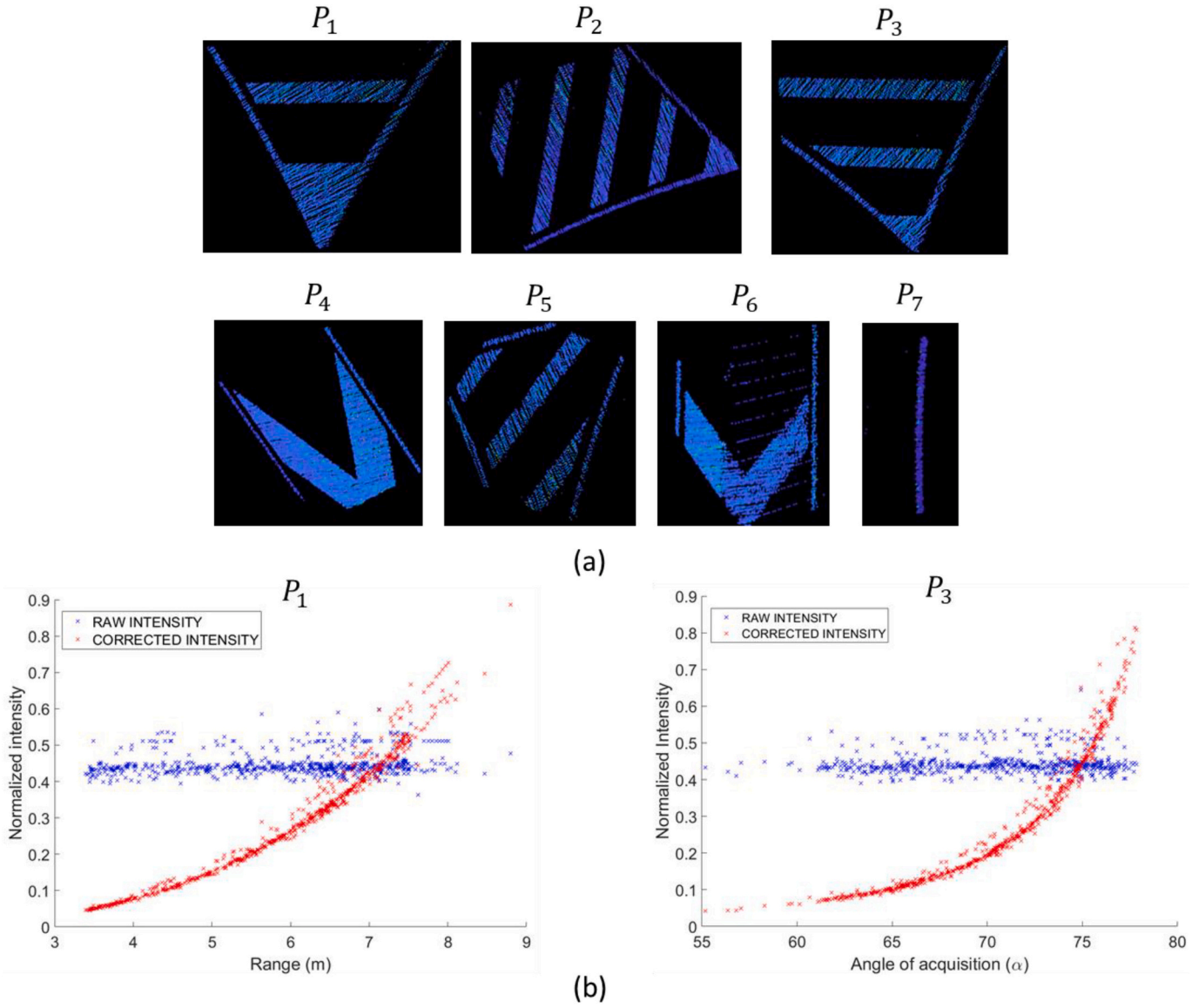

Fig. 6. (a) Subset of point clouds from road markings used to analyse the radiometric behaviour of the VLP-32C scanner. **(b)** The normalized raw and corrected intensities are plotted against range (left) and angle of acquisition (right).

algorithms are also tested: (1) Trust-region, and (2) Levenberg-Marquardt. This leads to four models where the difference between both fitting algorithms is negligible. Therefore, Trust-Region algorithm is employed to plot the resulting models in Fig. 7. The corresponding adjustment metrics are shown in Table 4, where it can be seen that LAR method obtains a better fit in terms of R-square and a smaller Root Mean Squared Error (RMSE).

To validate the performance of the model, two experiments were done. The objective of the first experiment was to validate whether the model was able to reliably show areas with high degradation. First, the

Table 3
Pairwise Pearson's linear correlation between (R, α) parameters and both raw and corrected intensities.

Variable 1	Variable 2	Pearson's linear correlation
R	I_{raw}	−0.0259
	$I_{corrected}$	0.9348
α	I_{raw}	0.0115
	$I_{corrected}$	0.7439

selected model was applied to the point cloud data associated to dataset 3 (Ávila). Then, the R_L values were manually inspected, and a total of 15 coordinates of areas with high degradation (R_L values under 100 mcd/m^2/lx) were annotated as a set of points $(P_1, \ldots, P_{15})$. Note that this manual annotation was carried out with no knowledge of the actual state of the road marking, as the 3D point cloud did not have colour information available. Subsequently, those coordinates were measured with the retroreflectometer, and the results (average of three consecutive measurements on the same point, slightly lifting and posing the retroreflectometer again between measurements) were annotated, and they are shown in Table 5. It can be seen that the model exhibits high reliability in showing areas with high degradations, as only two of the fifteen points were above 100 mcd/m^2/lx, and they were points with a R_L value close to the limit that was set for the manual inspection of the point clouds.

The second experiment computed the average error and standard deviation between the model output and the R_L values measured by staff from the road maintenance company with the retroreflectometer on the dataset 3 (Ávila). The objective of this experiment was to quantify the accuracy of the degradation model with a set of R_L measurements in a dataset that had not been used for fitting the model. First, a set of 48 R_L measurements (with the same averaging procedure that was described in the previous experiment) were recorded together with their GPS position. Note that the minimum and maximum R_L values resulting from the measurements are 14 mcd/m^2/lx and 520 mcd/m^2/lx respectively, and the and average standard deviation of the R_L measurements on the same location is 10.88 mcd/m^2/lx. Then, those positions were inspected in the 3D point cloud, and the estimated R_L values, obtained by applying the degradation model, were retrieved for each position. Finally, the values recorded with the retroreflectometer and with the degradation model were compared. As expected, the average error is low (3.26 mcd/m^2/lx) and the standard deviation is higher (72.78 mcd/m^2/lx).

4.3. Data visualization

Following the point cloud processing workflow defined in Section 0 (Fig. 5), an output consisting of two .csv files is obtained. The first file contains data for visualization, embedded in a Nx4 matrix with the degradation data of N road marking points within the input 3D point cloud. For each point, the file contains its (x,y) geographic coordinates,

Table 4
Model adjustment metrics.

Robust method	Model	R-square	RMSE (mcd/m^2/lx)
LAR	$R_L = 1990\ I_{raw}^{2.983}$	0.956	19.13
Bisquare	$R_L = 3577\ I_{raw}^{3.558}$	0.762	44.47

Table 5
R_L values measured with the retroreflectometer in field, for the set of highly degraded coordinates.

Point Index	R_L value	Point Index	R_L value
P_1	32.33	P_9	17.66
P_2	31.00	P_{10}	52.00
P_3	40.66	P_{11}	123.00
P_4	47.33	P_{12}	32.66
P_5	60.00	P_{13}	71.00
P_6	88.25	P_{14}	23.33
P_7	39.33	P_{15}	56.66
P_8	126.00		

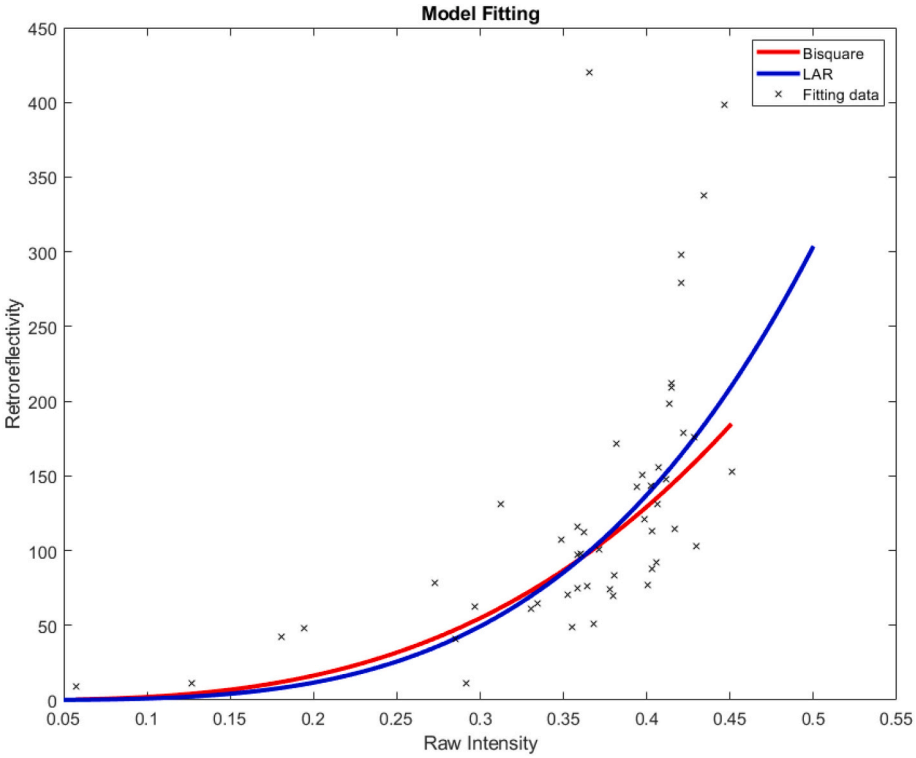

Fig. 7. Degradation models.

the R_L value, and a degradation index that allows for a qualitative visualization of the data and is defined in Table 6. The data can be easily shown in any GIS software. In this case, it is displayed over an orthophoto of the area of study using QGIS (Fig. 8).

The second file contains data that may assist the decision support for corrective and preventive maintenance. Given the specifications of the end-users of this work, it is relevant to know the percentage of points with greater degradation (degradation indices equal to 1) in road sections of specified length in order to make decisions regarding road marking repainting. For that reason, the N points that are part of the output are split in M clusters, each of them corresponding to a road section of 100 m of length. For each section, the following data is recorded:

1. The initial kilometric point of the section.
2. The total number of analysed points in the section.
3. The percentage of highly degraded ($R_L \leq 100$) points.

This way, areas that surpass a percentage of highly degraded points (which is given by the end user) can be easily located for further inspection and more efficient decision making.

5. Discussion

The presented methodology can be divided into two well-differentiated parts. First, the radiometric behaviour of the VLP-32C laser scanner was studied, finding that there is no influence of distance and angle of acquisition on the raw intensity values of the 3D point clouds, at least in the context of an application for road marking detection and analysis. While this simplifies the problem – finding a function that estimates the coefficient of retroreflected luminance given the intensity attribute of a point -, it is important to note that this analysis is only applicable to the laser employed in this work. The same application on point clouds acquired with a different laser scanner would need a similar approach, as the way the intensity attribute is internally corrected and discretized is typically unknown by the user, and dependent on the manufacturer. It is also relevant to highlight the empirical and application-oriented nature of this work, as case study data has only been recorded in the field, at different times of the year, with no previous analysis in laboratory.

A second methodological block is focused on the exploitation of this first result to obtain degradation maps of the road markings, to support preventive and corrective maintenance tasks. Qualitatively, the resulting visualization of the data is intuitive and shows a clear picture of the global degradation of the road markings and highly degraded areas. Quantitatively, the selected degradation model is able to estimate the retroreflectivity of an area but with a high standard deviation for individual measurements. This is due to the noisy nature of the point cloud data, as well as the R_L measurements in the field, which may vary considerably when moving the retroreflectometer a few centimetres. For that reason, the retroreflective measurements, as shown in Table 5, are the result of averaging three individual measurements of the same area. Another limitation of this process can be seen in Fig. 8b. Note that there is a section on the interior edge of the curve with no degradation data. This is due to errors in the road marking segmentation process, where points with high degradation and therefore low intensity cannot be properly segmented. This sets a harder problem to solve in the segmentation side of the process, which is out of the scope of this work, as a fully automated segmentation process that is robust to lines that have lost practically all their retroreflective properties will require adding reconstruction and/or knowledge and context-based algorithms to the workflow. However, if the data is visualized by a user with previous knowledge, it is relatively easy to infer that, as in the case exemplified, with an interior edge of a curve that shows high degradation and loss of data in between, the missing data will also correspond to high degradation.

Table 6
Degradation indices defined for a qualitative visualization of the degradation map.

Degradation index	R_L value
1	$R_L \leq 100$
2	$100 < R_L \leq 150$
3	$150 < R_L \leq 200$
4	$R_L > 200$

The outputs of this work include data for generating degradation maps, which can be visualized in GIS software, and also data to assist predictive and corrective maintenance activities. In this case, the percentage of highly degraded points per 100 m of road section is recorded. Given the feedback of the end-users of this work, sections with >10% of these points should generate warnings, so corrective maintenance can be considered. It is clear that the length of the section, the percentage of degraded points or the R_L indexing are parameters that can be easily modified and adapted to the needs and requisites of different end-users.

6. Conclusions

This paper presents an application to compute road marking degradation maps to support preventive and corrective maintenance tasks, using 3D point clouds acquired with a Mobile LiDAR System. The MLS employed is a Phoenix Scout Ultra 32, equipped with a low-cost Velodyne VLP-32C laser scanner. Data for this work were collected in three different locations in Spain, at different times of the year. First, a correction for the intensity value of the 3D point cloud was proposed, following the existing literature, which stated that the intensity attribute was influenced by the distance between the laser scanner and the acquired point, and the angle of acquisition. This analysis showed that this theoretical correction was not necessary for the sensor. In fact, there was no influence of the studied parameters on the recorded intensity values. This allowed the definition of a model to estimate the coefficient of retroreflected luminance (night visibility, R_L) using only the intensity attribute of the point cloud. Then, the model was validated using data recorded in the field by a retroreflectometer, finding that it is able to reliably detect areas with a high level of degradation. It also has a low average error, but R_L values are noisy along the point cloud.

With the proposed model, it is possible to generate road marking degradation marks that can be visualized in GIS software. Furthermore, the requisites of the end-users of this application can be added to the results by highlighting road sections in need of corrective maintenance. Therefore, this application can save resources in road marking maintenance activities. Measuring all the road markings with a static retroreflectometer is unfeasible, and still extracting a small sample of data from a road section is a slow task. With both a dynamic retroreflectometer and a MMS, a high number of measurements can be extracted, and the data can be collected at conventional driving speeds, with no need for maintenance staff to measure outside of the vehicle (reducing risks and roadblocks). However, MMS offer more versatility, and the collected data can be applied for multiple maintenance-related applications, thus offering a strategic advantage over dedicated equipment.

Future work will include the integration of robust road marking segmentation algorithms. Although it was not part of the scope of this work, a reliable degradation map obtained in the context of a fully automated methodology will likely need to include a Deep Learning based architecture for road marking segmentation. Furthermore, predictive maintenance should be considered as well, by studying degradation models for road markings over time and gathering data from the same areas at different time epochs, estimating the best maintenance strategy. The positive results achieved with this work will encourage further research on the study of the capability of different LiDAR sensors for road marking degradation analysis, and different materials and casuistries will be tested. Finally, the case study data can be augmented by

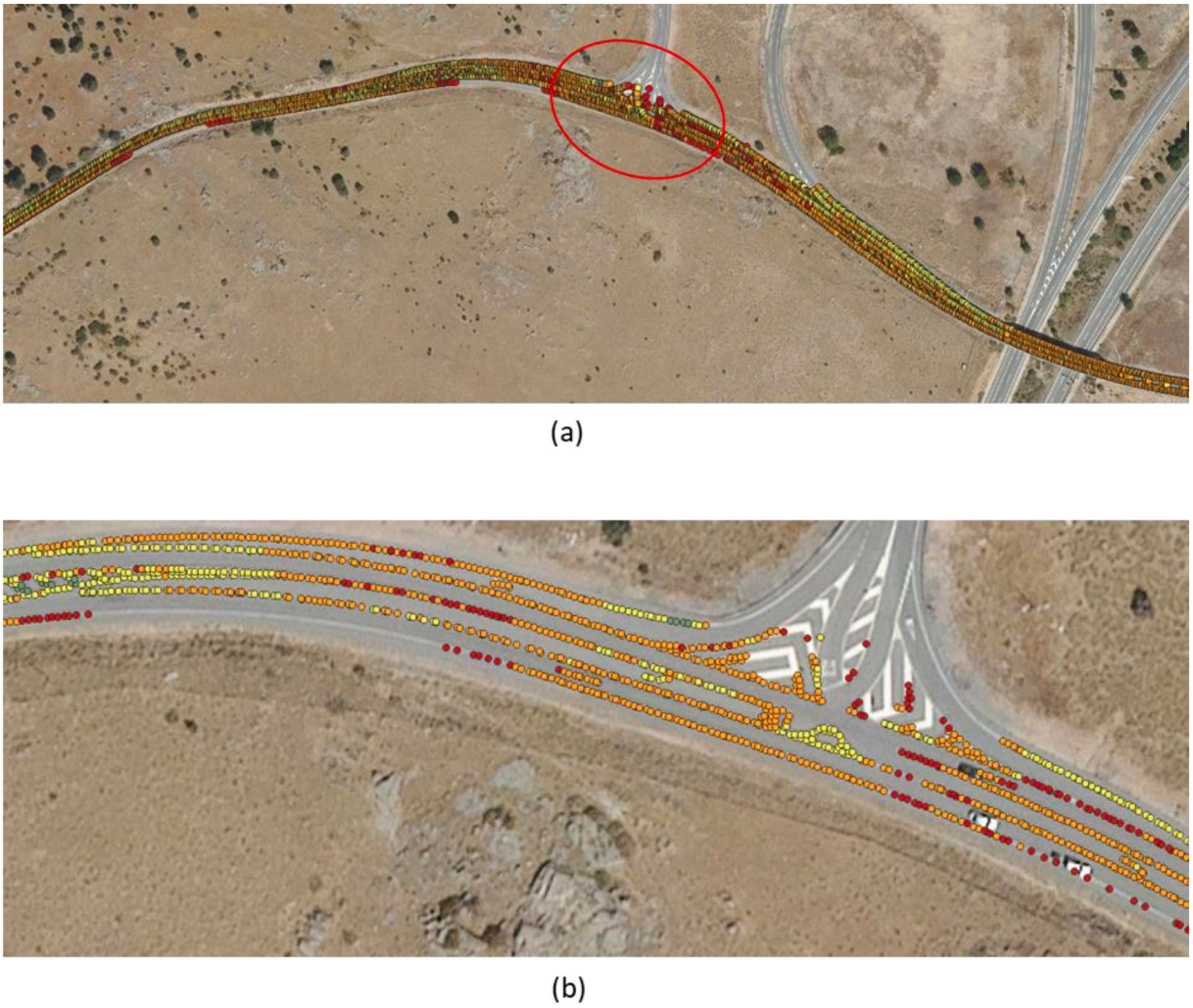

Fig. 8. **(a)** Visualization of the degradation map. Red, orange, yellow and green points correspond to degradation indices 1, 2, 3 and 4, respectively. **(b)** Detailed view of the degradation map. (For interpretation of the references to colour in this figure legend, the reader is referred to the web version of this article.)

adding more data points and considering rainy conditions, so variations in the developed models can be taken into account.

Declaration of Competing Interest

The authors declare that they have no known competing financial interests or personal relationships that could have appeared to influence the work reported in this paper.

Acknowledgments

The research leading to these results received funding from the Strategic Program of Research Consortia National Business (CDTI) at the INROAD 4.0 project (IDI-20181117) under the call 2018 for the strategic program CIEN. This work has been partially supported by the Spanish Ministry of Science and Innovation through the grant FJC2018-035550-I funded by MCIN/AIE/ 10.13039/501100011033.

References

[1] European Commission, EU Transport in Figures - Statistical Pocketbook 2021, 2021, https://doi.org/10.2832/27610.
[2] K. Williams, M.J. Olsen, G.V. Roe, C. Glennie, Synthesis of transportation applications of mobile LIDAR, Remote Sens. 5 (2013) 4652–4692, https://doi.org/10.3390/rs5094652.
[3] H. Guan, J. Li, S. Cao, Y. Yu, Use of mobile LiDAR in road information inventory: a review, Int. J. Image Data Fusion 7 (2016) 219–242, https://doi.org/10.1080/19479832.2016.1188860.
[4] S. Gargoum, K. El-Basyouny, Automated extraction of road features using LiDAR data: A review of LiDAR applications in transportation, in: 4th International Conference on Transportation Information and Safety, 2017, pp. 563–574, https://doi.org/10.1109/ICTIS.2017.8047822.
[5] L. Ma, Y. Li, J. Li, C. Wang, R. Wang, M.A. Chapman, Mobile laser scanned point-clouds for road object detection and extraction: a review, Remote Sens. 10 (2018) 1–33, https://doi.org/10.3390/rs10101531.
[6] M. Soilán, A. Sánchez-Rodríguez, P. del Río-Barral, C. Perez-Collazo, P. Arias, B. Riveiro, Review of laser scanning technologies and their applications for road and railway infrastructure monitoring, Infrastructures. 4 (2019) 58, https://doi.org/10.3390/infrastructures4040058.
[7] E. Che, M.J. Olsen, J. Jung, Efficient segment-based ground filtering and adaptive road detection from mobile light detection and ranging (LiDAR) data, Int. J. Remote Sens. 42 (2021) 3633–3659, https://doi.org/10.1080/01431161.2020.1871095.
[8] A. Holgado-Barco, B. Riveiro, D. González-Aguilera, P. Arias, Automatic inventory of road cross-sections from mobile laser scanning system, computer-aided civil and infrastructure, Engineering. 32 (2017) 3–17, https://doi.org/10.1111/mice.12213.
[9] A. Holgado-Barco, D. González-Aguilera, P. Arias-Sanchez, J. Martinez-Sanchez, Semiautomatic extraction of road horizontal alignment from a mobile LiDAR system, Computer-Aided Civil Infrastruct. Eng. 30 (2015) 217–228, https://doi.org/10.1111/mice.12087.
[10] J. Wang, R. Lindenbergh, M. Menenti, SigVox – A 3D feature matching algorithm for automatic street object recognition in mobile laser scanning point clouds, ISPRS J. Photogramm. Remote Sens. 128 (2017) 111–129, https://doi.org/10.1016/j.isprsjprs.2017.03.012.
[11] H. Matsumoto, Y. Mori, H. Masuda, Extraction of guardrails from mms data using convolutional neural network, Int. J. Autom. Technol. 15 (2021) 258–267, https://doi.org/10.20965/ijat.2021.p0258.

[12] D. Shokri, H. Rastiveis, W.A. Sarasua, A. Shams, S. Homayouni, A robust and efficient method for power lines extraction from Mobile LiDAR point clouds, PFG - J. Photogramm. Remote Sens. Geoinform. Sci. 89 (2021) 209–232, https://doi.org/10.1007/s41064-021-00155-y.

[13] Y. Yu, J. Li, H. Guan, F. Jia, C. Wang, Learning hierarchical features for automated extraction of road markings from 3-D mobile LiDAR point clouds, IEEE J. Select. Top. Appl. Earth Observ. Remote Sens. 8 (2015) 709–726, https://doi.org/10.1109/JSTARS.2014.2347276.

[14] H. Guan, J. Li, S. Member, Y. Yu, Z. Ji, C. Wang, Using mobile LiDAR data for rapidly updating road markings, IEEE Trans. Intell. Transp. Syst. 16 (2015) 2457–2466, https://doi.org/10.1109/TITS.2015.2409192.

[15] C. Wen, X. Sun, J. Li, C. Wang, Y. Guo, A. Habib, A deep learning framework for road marking extraction, classification and completion from mobile laser scanning point clouds, ISPRS J. Photogramm. Remote Sens. 147 (2019) 178–192, https://doi.org/10.1016/j.isprsjprs.2018.10.007.

[16] L. Ma, S. Member, Y. Li, G. Student Member, J. Li, S. Member, Y. Yu, J. Marcato Junior, W. Nunes Gonçalves, M.A. Chapman, J., Li Lingfei Ma, Capsule-based networks for road marking extraction and classification from mobile LiDAR point clouds, IEEE Trans. Intell. Transp. Syst. 22 (2021) 1981–1995, https://doi.org/10.1109/TITS.2020.2990120.

[17] A.G. Kashani, M.J. Olsen, C.E. Parrish, N. Wilson, A review of LIDAR radiometric processing: from ad hoc intensity correction to rigorous radiometric calibration, Sensors (Switzerland). 15 (2015) 28099–28128, https://doi.org/10.3390/s151128099.

[18] S. Kaasalainen, A. Krooks, A. Kukko, H. Kaartinen, Radiometric calibration of terrestrial laser scanners with external reference targets, Remote Sens. 1 (2009) 144–158, https://doi.org/10.3390/RS1030144.

[19] A. Pesci, G. Teza, Effects of surface irregularities on intensity data from laser scanning: an experimental approach, Ann. Geophys. 51 (2009), https://doi.org/10.4401/AG-4462.

[20] B. Höfle, N. Pfeifer, Correction of laser scanning intensity data: data and model-driven approaches, ISPRS J. Photogramm. Remote Sens. 62 (2007) 415–433, https://doi.org/10.1016/j.isprsjprs.2007.05.008.

[21] S. Kaasalainen, A. Jaakkola, M. Kaasalainen, A. Krooks, A. Kukko, Analysis of incidence angle and distance effects on terrestrial laser scanner intensity: search for correction methods, Remote Sens. 3 (2011) 2207–2221, https://doi.org/10.3390/RS3102207.

[22] C. Ai, Y.J. Tsai, An automated sign retroreflectivity condition evaluation methodology using mobile LIDAR and computer vision, Transp. Res. C: Emerg. Technol. 63 (2016) 96–113, https://doi.org/10.1016/j.trc.2015.12.002.

[23] A.F. Habib, A.P. Kersting, A. Shaker, W.Y. Yan, Geometric calibration and radiometric correction of LiDAR data and their impact on the quality of derived products, Sensors 2011 (11) (2011) 9069–9097, https://doi.org/10.3390/S110909069.

[24] T.E. Burghardt, R. Popp, B. Helmreich, T. Reiter, G. Böhm, G. Pitterle, M. Artmann, Visibility of various road markings for machine vision, Case Studies in Construction Materials. 15 (2021), https://doi.org/10.1016/J.CSCM.2021.E00579.

[25] D. Babić, M. Fiolić, D. Žilioniene, M.T. Ing, A. Daiva Žilioniene, Evaluation of static and dynamic method for measuring retroreflection of road markings, Gradevinar. 69 (2017) 907–914, https://doi.org/10.14256/JCE.2010.2017.

[26] M.J. Olsen, C. Parrish, E. Che, J. Jung, J. Greenwood, Lidar for maintenance of pavement reflective markings and retroreflective signs, Oregon. Dept. of Transportation (2018), https://doi.org/10.21949/1503647.

[27] Velodyne LiDAR Inc, Velodyne LiDAR VLP-32C - Specifications Sheet. https://www.mapix.com/wp-content/uploads/2018/07/63-9378_Rev-D_ULTRA-Puck_VLP-32C_Datasheet_Web.pdf, 2018 (accessed April 18, 2022).

[28] M. Bijelic, T. Gruber, W. Ritter, A benchmark for lidar sensors in fog: is detection breaking down?, in: IEEE Intelligent Vehicles Symposium Institute of Electrical and Electronics Engineers Inc., 2018, pp. 760–767, https://doi.org/10.1109/IVS.2018.8500543.

[29] Ministerio de Fomento Gobierno de España, Guía para el proyecto y ejecución de obras de señalización horizontal. https://cdn.mitma.gob.es/portal-web-drupal/carreteras/normativa/guia_sh.pdf, 2012 (accessed April 24, 2021).